



# Influence of cerium treatment on inclusion modification and as-cast microstructure of high-strength low-alloy steel

Ru-ming Geng<sup>1</sup> · Jing Li<sup>1</sup> · Cheng-bin Shi<sup>1</sup>

Received: 9 August 2021 / Revised: 9 September 2021 / Accepted: 12 September 2021 / Published online: 13 February 2022  
© China Iron and Steel Research Institute Group 2022

## Abstract

The influence of cerium treatment on the inclusion evolution and as-cast microstructure of high-strength low-alloy steel was investigated. Properties including the inclusions characteristics, element distribution, and the in situ solidification were analyzed by scanning electron microscopy, energy-dispersive spectroscopy, and high-temperature confocal laser scanning microscopy, respectively. The results indicated that, after the addition of Ce, the  $\text{Al}_2\text{O}_3$  inclusions evolved to form  $\text{Ce}_2\text{O}_2\text{S}$  and  $\text{CeAlO}_3$  inclusions, which exhibited a decrease in size alongside corresponding increase in their number density. The equiaxed grain ratio exhibited by the as-cast microstructure increased significantly upon the addition of Ce, while a reduction in the segregation and a corresponding increase in the homogeneity of the carbon distribution within the as-cast microstructure were also achieved. The results of the in situ observation of the solidification suggested that the addition of Ce significantly reduced the solidification temperature range, thus reducing the carbon segregation. The nucleation effect imparted by  $\text{Al}_2\text{O}_3$ ,  $\text{Ce}_2\text{O}_2\text{S}$ , and  $\text{CeAlO}_3$  on the  $\delta$ -Fe formation was discussed in the context of the disregistry theory, which revealed that the formation of a large number of fine  $\text{Ce}_2\text{O}_2\text{S}$  inclusions promoted  $\delta$ -Fe formation via heterogeneous nucleation.

**Keywords** Ce treatment · Non-metallic inclusion · As-cast microstructure · In situ observation · Disregistry theory

## 1 Introduction

High-strength low-alloy (HSLA) steels have been used extensively owing to their high strength and enhanced impact toughness. Their numerous applications cover a variety of fields including buildings, bridges, module vehicles, pressure vessels, and pipelines [1, 2]. With the development of high strength and lightweight components, higher mechanical properties of HSLA steel are required, such as strength, impact toughness, and welding performance, which are greatly influenced by the composition and morphology of the non-metallic inclusions [3].

$\text{Al}_2\text{O}_3$  inclusions are generally considered to be detrimental to steel quality as they are formed as oxidation products in Al-sacrificed steel. To avoid the detrimental effects of  $\text{Al}_2\text{O}_3$  inclusions in steel, calcium treatment is

commonly used to modify alumina inclusions to form calcium aluminum inclusions, which exhibit a lower melting point [4–6]. In addition to Ca treatment, rare earth elements can also modify  $\text{Al}_2\text{O}_3$  inclusions. Ren and Zhang [7] reported that as the Ce content in steel increased, the inclusion compositions varied as follows:  $\text{Al}_2\text{O}_3 \rightarrow \text{CeAlO}_3 \rightarrow \text{Ce}_2\text{O}_2\text{S} \rightarrow \text{Ce}_2\text{O}_2\text{S} + \text{CeS}$ . Owing to their high melting point and low mismatch relative to acicular ferrite, rare earth inclusions are also applied to improve the welding performance of steel, which is known as “rare earth oxide metallurgy” [8–10].

Moreover, rare earth additions can also play a role in refining the as-cast microstructure, which is beneficial to the overall formability and mechanical properties exhibited by the steel. Wang et al. [11] demonstrated that the addition of a small amount of Ce in super-austenitic stainless steel accelerated  $\delta$ -Fe nucleation within the interdendritic solute-rich liquid, refined the solidified structure, and also reduced Mo and Cr segregation. Torkamani et al. [12] also reported that the addition of Ce in low carbon cast Nb-microalloyed steel induced smaller and more spherical

✉ Jing Li  
lijing@ustb.edu.cn

<sup>1</sup> State Key Laboratory of Advanced Metallurgy, University of Science and Technology Beijing, Beijing 100083, China

inclusions. It was also found that a finer microstructure was obtained, which contributed positively to the enhancement of the impact toughness by approximately 60%. The grain refinement of various steels through the addition of rare earth elements has also been investigated by a large number of researchers [11, 13–15].

In this study, the influence of Ce treatment on the inclusion modification and as-cast microstructure of HSLA steel was investigated. Through experimental observation and thermodynamic calculations, the formation mechanisms of oxide inclusions with Ce addition and the nucleation effect of these inclusions during the solidification of Al-sacrificed steel were investigated. In addition, the effect of Ce on carbon segregation and in situ solidification observation were also studied.

## 2 Experimental

### 2.1 Sample preparation

Two ingots were produced via melting of the raw materials in a 50 kg vacuum induction furnace. The raw material was heated to 1873 K, at which point the aluminum was added to decrease the oxygen content. After deoxidation, 52.5 g of a Ce–Fe alloy (with a Ce mass fraction of 20% and a total impurity mass fraction for carbon, sulfur, oxygen and phosphorus below 0.02%) was added to the liquid steel. Following this, the liquid steel was cast into a square billet, designated ingot B, with dimensions of 150 mm × 150 mm × 300 mm. For comparison, a second ingot, ingot A, was cast in the same manner without the addition of Ce–Fe alloy. A plate with a thickness of 20 mm was cut along the cross section from about 40 mm away from the bottom of the ingot to evaluate the solidification microstructure. Following this, a square plate of 85 mm × 85 mm × 20 mm and a metallographic sample of 8 mm × 8 mm × 10 mm were cut to facilitate segregation analysis and inclusion observation, respectively.

### 2.2 Compositional analysis

Steel samples were machined from each ingot to analyze the Ce content using inductively coupled plasma mass spectrometry (ICP-MS). Polished rods, 5 mm in diameter and 7 mm in length, were created to determine the total O (TO) and N contents using an oxygen, nitrogen and hydrogen analyzer (HORIBA EMGA-830, Japan). The C and S contents were determined using a carbon and sulfur analyzer (HORIBA EMIA-920V2, Japan). The remaining element contents were evaluated using an optical emission spectrometer (Thermo Fisher ARL-8860, USA).

Comprehensive chemical compositions of the two experimental ingots are listed in Table 1.

### 2.3 Inclusion characterization and microstructural observation

The as-cast microstructures of the two experimental ingots were revealed via etching using a hydrochloric acid aqueous solution (HCl:H<sub>2</sub>O = 1:1) for 15 min in a constant-temperature water bath at 80 °C. During the segregation analysis, the carbon segregation along the transverse portion of the steel was observed using an original position analysis apparatus (OPA-200, NCS Testing Technology Co., Ltd., Beijing, China), with a scanning area of 70 mm × 70 mm. The steel samples were polished using silicon carbide papers and diamond paste to facilitate an analysis of the inclusion characteristics and evolution by scanning electron microscopy (SEM, FEI Quanta-250, FEI Corporation, Hillsboro, OR, USA) equipped with an energy-dispersive spectrometer (EDS, XFlash 5030, Bruker, Germany). The instrument was operated at an acceleration voltage of 20 kV. Any inclusion larger than 0.5 μm was detected using an INCA Steel automatic detection system for non-metallic inclusion (EVO 18, ZEISS, Germany) to analyze the size distribution exhibited by the inclusions, with a scanning area of 5 mm × 5 mm.

### 2.4 In situ observation

The materials were machined to form specimens of 5 mm in diameter and 3 mm in length. Prior to the experiment, the specimens were ground and polished before being mounted in cylindrical alumina crucibles. The in situ observation of the solidification was performed by high temperature confocal laser scanning microscopy (HTCLSM) under a pure Ar protective atmosphere. Two specimens were heated to 1550 °C at a heating rate of 100 °C/min. Once the samples reached the predetermined temperature, they were held there for 3 min to ensure complete homogeneous melting, and then cooled to 25 °C at a cooling rate of 50 °C/min.

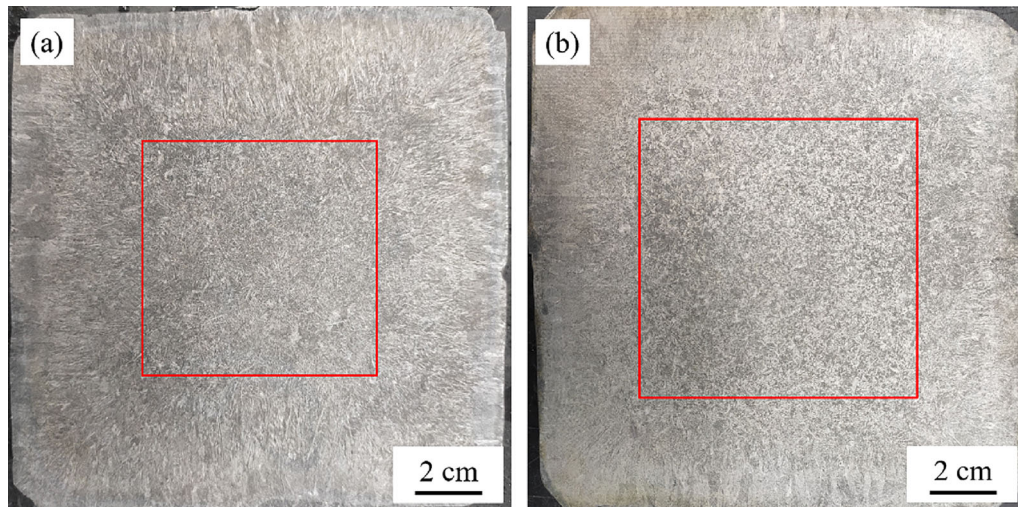
## 3 Results and discussion

### 3.1 As-cast microstructure

The as-cast microstructures of the two experimental ingots are shown in Fig. 1, with the equiaxed zone identified as within the red boundary. It was observed that, compared with ingot A, ingot B exhibited a larger equiaxed zone alongside a reduced columnar crystal area. Along the horizontal plane, the ratio of the equiaxed zone increased

**Table 1** Chemical compositions of each experimental ingots (wt.%)

Ingot	C	Si	Mn	Cr	Al	Ti	V
Ingot A	0.12	0.30	1.58	0.31	0.010	0.018	0.075
Ingot B	0.12	0.30	1.51	0.31	0.019	0.016	0.069
Ingot	Nb	Mo	B	S	O	N	Ce
Ingot A	0.047	0.15	0.0017	0.0051	0.0022	0.0031	0
Ingot B	0.051	0.15	0.0018	0.0059	0.0016	0.0030	0.0065

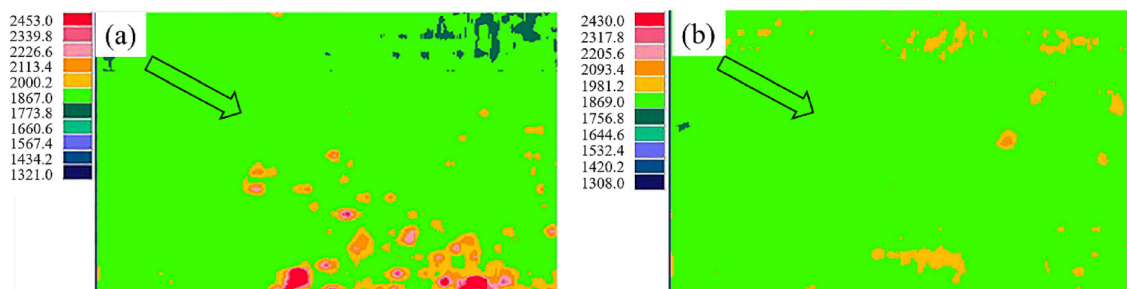
**Fig. 1** Solidification structure exhibited by two experimental ingots. **a** Ingot A; **b** ingot B

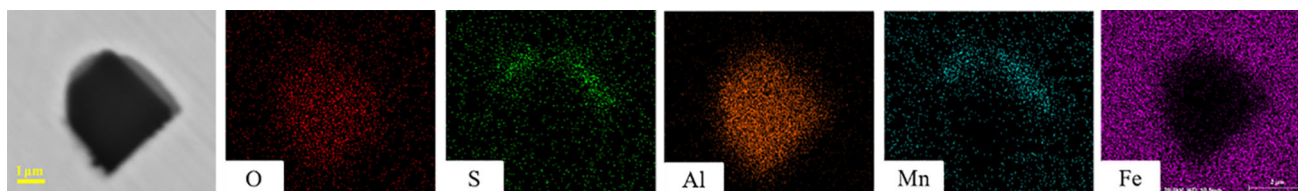
from 46% to 55%. It has been suggested that a large equiaxed zone ratio decreases the volume of defects within the as-cast ingot while also mitigating element segregation [16].

Figure 2 shows a two-dimensional contour mapping which reveals the carbon distribution throughout ingots A and B. In Fig. 2, the carbon concentration is depicted through varying colors. Through a comparison of Fig. 2a and b, it was observed that the addition of Ce imparted a reduction in the segregation alongside a more homogeneous distribution of carbon throughout the steel.

### 3.2 Characteristics of inclusions

Element mappings of the typical inclusions in ingot A are shown in Figs. 3 and 4. Using SEM-EDS, it was possible to classify the typical inclusions within ingot A into three distinct categories: (a) an  $\text{Al}_2\text{O}_3$  core surrounded by MnS (Figs. 3 and 4a); (b) individual  $\text{Al}_2\text{O}_3$  inclusions (Fig. 4b); (c) individual MnS inclusions. As a common source of deoxidation in Al-sacrificed steel,  $\text{Al}_2\text{O}_3$  inclusions are considered to be detrimental to both the quality and castability of steels, owing to their significant hardness

**Fig. 2** Carbon distribution mapping of ingots A and B. **a** Ingot A; **b** ingot B. Black arrow indicates ingot center



**Fig. 3** Element mappings of typical inclusions present in ingot A:  $\text{Al}_2\text{O}_3 + \text{MnS}$

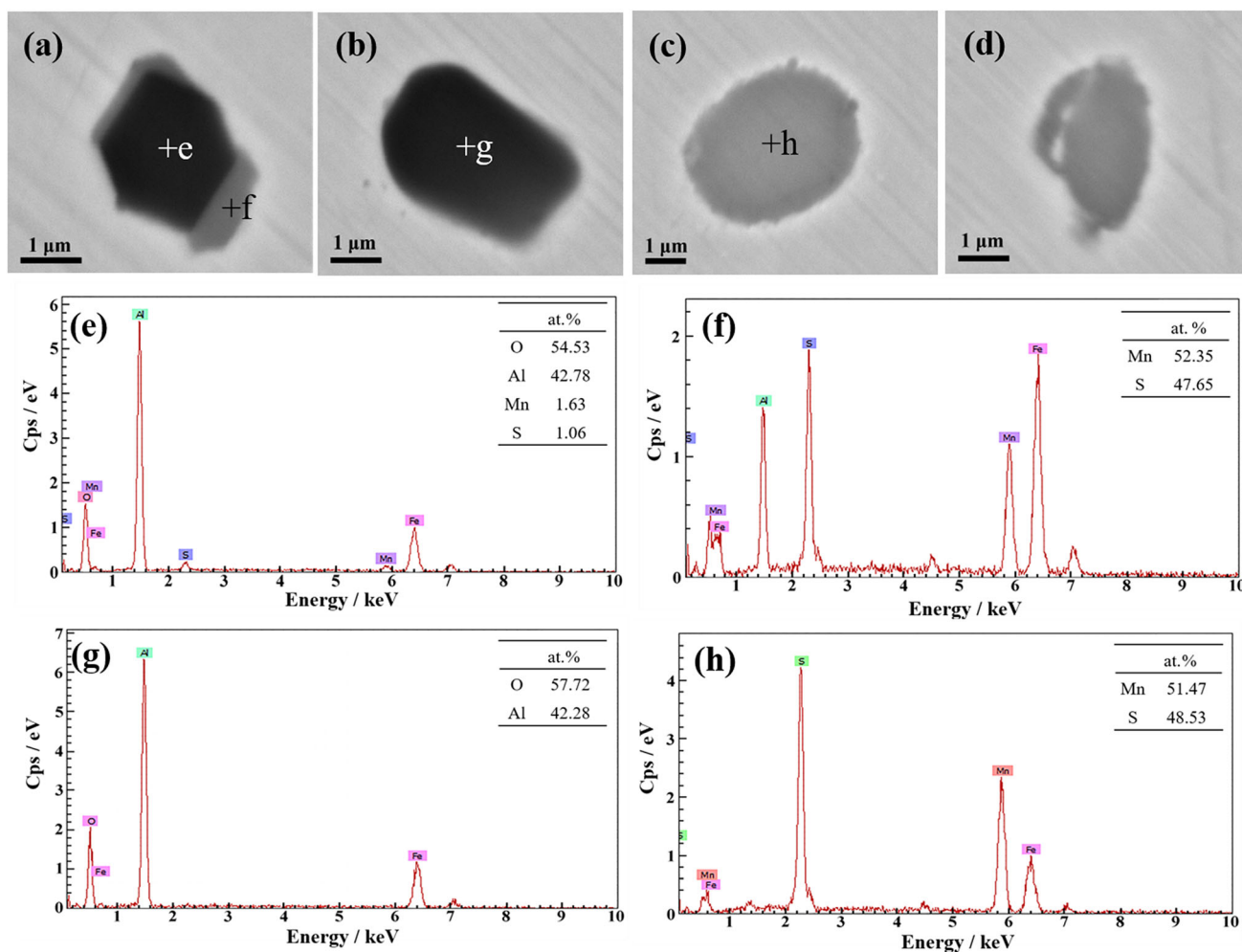


**Fig. 4** Backscattered electron images (a–d) and EDS results (e–h) obtained from typical inclusions observed in ingot A. **a**  $\text{Al}_2\text{O}_3 + \text{MnS}$ ; **b**  $\text{Al}_2\text{O}_3$ ; **c, d**  $\text{MnS}$ ; **e–h** EDS spectrums correspond to areas marked in a–c, respectively

[17]. In addition to Ca treatment [18, 19], the addition of rare earth in steel can also modify the  $\text{Al}_2\text{O}_3$  inclusions. The backscattered electron (BSE) images and EDS results obtained from the typical inclusions found in ingot B (Ce addition) are shown in Fig. 5. SEM–EDS identified these typical inclusions as either  $\text{Ce}_2\text{O}_3\text{S} + \text{MnS}$  complex inclusions (Fig. 5a) or  $\text{CeAlO}_3 + \text{MnS}$  inclusions (Fig. 5b). More than 200 rare earth inclusions present in ingot B were analyzed, and the results indicated that the relative proportions of the  $\text{Ce}_2\text{O}_3\text{S}$  and  $\text{CeAlO}_3$  inclusions were 65.9% and 34.1%, respectively, as shown in Fig. 6.

Figure 7 shows the size distribution of inclusions in ingots A and B. It can be observed that the inclusions were significantly finer in the steel with the added Ce. The number proportion of inclusions smaller than 2  $\mu\text{m}$  in diameter increased from 4.0% in ingot A to 54.6% in ingot B, while the number proportion of inclusions larger than 5  $\mu\text{m}$  was reduced by 26.9%. In addition, the number density of the inclusions increased from 19.80 to 41.96  $\text{mm}^{-2}$  upon the addition of Ce, while the average diameter of these inclusions decreased from 4.51 to 2.32  $\mu\text{m}$ , as shown in Fig. 8.

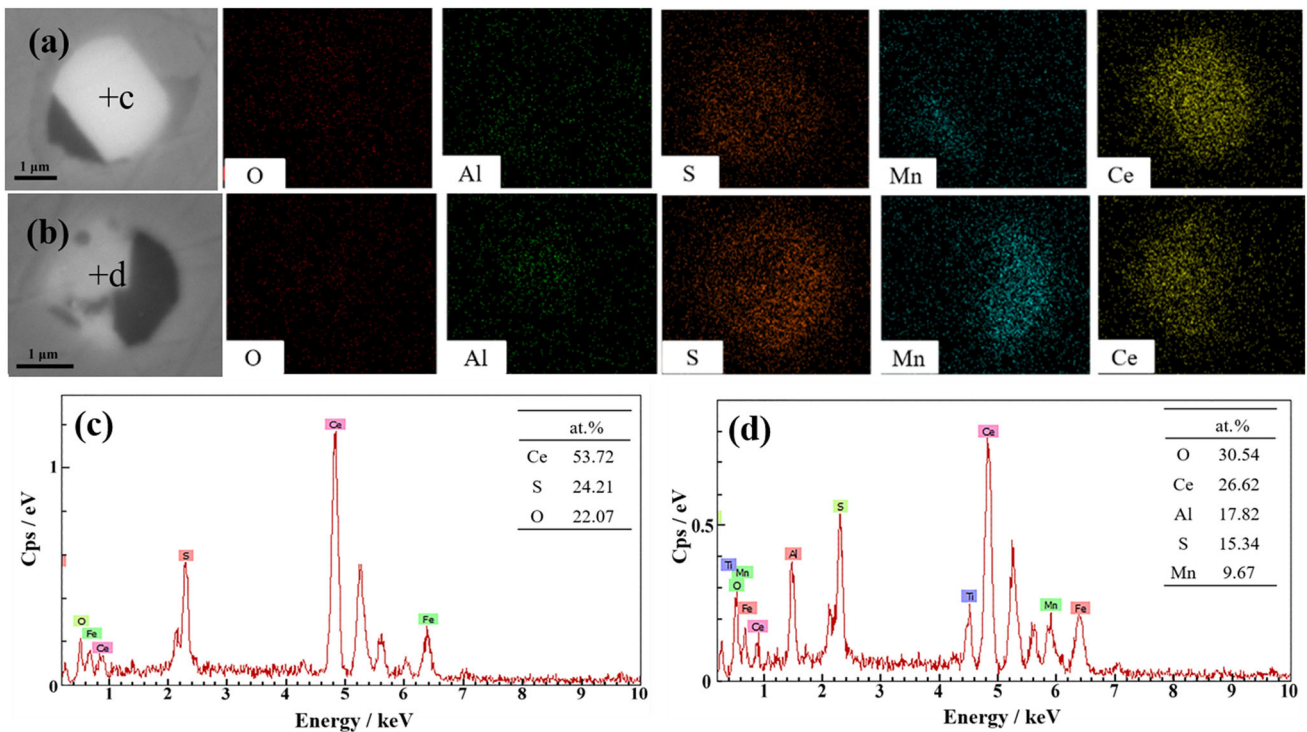


**Fig. 5** SEM images and EDS profiles of typical inclusions found in ingot B. **a** Ce<sub>2</sub>O<sub>2</sub>S + MnS; **b** CeAlO<sub>3</sub> + MnS; **c, d** EDS profiles corresponding to areas marked in **a** and **b**, respectively

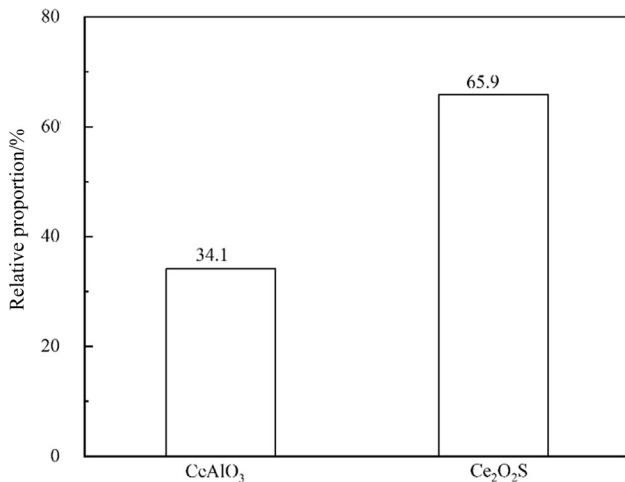


**Fig. 6** Relative proportion of CeAlO<sub>3</sub> and Ce<sub>2</sub>O<sub>2</sub>S inclusions in ingot B

### 3.3 Equilibrium thermodynamic calculation of inclusion formation

To evaluate the inclusion evolution, FactSage 8.0, with FSstel, FactPA, and FToxid databases, was used to analyze the equilibrium thermodynamic calculation performed in this study, as shown in Fig. 9. It was observed that, without the addition of Ce, Al<sub>2</sub>O<sub>3</sub> inclusions formed in the liquid steel in ingot A. In case of ingot B, Ce<sub>2</sub>O<sub>3</sub> and CeAlO<sub>3</sub>

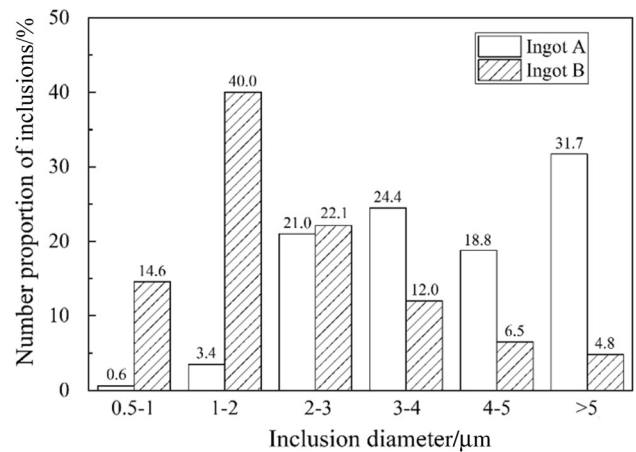
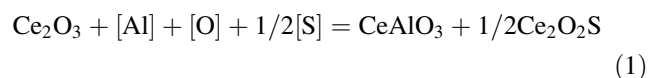


**Fig. 7** Size distribution of inclusions in ingots A and B

inclusions formed in liquid steel at 1600 °C. As the temperature decreased, Ce<sub>2</sub>O<sub>3</sub> was transformed to CeAlO<sub>3</sub> and Ce<sub>2</sub>O<sub>2</sub>S at 1545 °C, which can be expressed as Eq. (1).



### 3.4 In situ observation of solidification

The solidification behavior exhibited by steel exerts a significant influence on the as-cast structure and solute

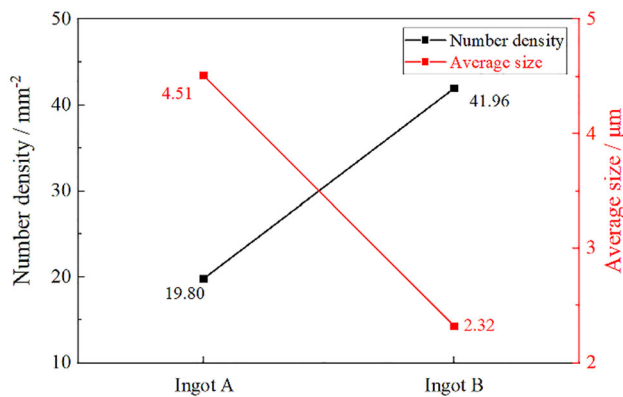


**Fig. 8** Number density and average diameter of inclusions in ingots A and B

element segregation. HTCLSM images gathered during the solidification process of ingot A are shown in Fig. 10. As shown in Fig. 10, when the temperature reached 1542.7 °C, the primary solid gradually formed within the liquid steel. As the temperature decreased, the formation of solid phase increased, while the retained liquid phase enriched with solute elements was distributed between the solid phases. As the temperature decreased to 1497.4 °C, the solidification process was completed and no retained liquid remained in the steel. A similar solidification process of ingot B was observed, as shown in Fig. 11.

Figure 12 shows the solid fraction change exhibited by ingots A and B throughout the solidification process. The solid fraction was calculated by evaluating the area fraction containing the solid phase in the field of view at various temperatures. It can be seen that with the addition of Ce, the liquidus temperature exhibited by ingot B decreased from 1542.7 to 1533.8 °C, while the solidus temperature increased from 1497.4 to 1511.1 °C. FactSage 8.0 was used to determine the solidification path of ingot A, as shown in Fig. 13. It can be seen that the liquid phase (L), L plus

ferrite ( $\delta$ ), L plus  $\delta$  and austenite ( $\gamma$ ), and L plus  $\gamma$  coexist in sequence throughout the solidification process. Thus, the results of the in situ observation indicate that the addition of Ce decreases the temperature required for the formation of  $\delta$ -Fe and also reduced the solidification temperature range. In addition, it should be noted that the temperature during the in situ observation was measured using a thermocouple positioned at the bottom of the crucible. As there was an inherent temperature discrepancy of approximately 20 °C between the crucible bottom and the sample surface [20], there was inconsistencies observation between the experimental and thermodynamic calculations.

The reduction in the liquidus temperature imparted by rare earth elements could be explained by their microalloying effect. As  $\delta$ -Fe nucleated and developed within the liquid steel, solute rare earth enrichment at the solid–liquid interface increased the energy barrier for solid phase growth, thus decreasing the liquidus temperature. Moreover, the formation of rare earth inclusions is beneficial in increasing the nucleation ratio of  $\delta$ -Fe and also reducing the solidification temperature range, which is described in further detail in Sect. 3.5. Reducing the solidification temperature range could significantly improve the segregation of the solute elements, which has been extensively reported in previous researches [21, 22].

### 3.5 Disregistry values between inclusions and $\delta$ -Fe

In comparison to ingot A, a larger equiaxed zone was observed in ingot B, which was significantly affected by heterogeneous nucleation [16, 23]. As described in Fig. 13,  $\delta$ -Fe was initially formed during the onset of solidification. Therefore, the effect of  $\text{Al}_2\text{O}_3$ ,  $\text{CeAlO}_3$ , and  $\text{Ce}_2\text{O}_2\text{S}$  on the promotion of  $\delta$ -Fe formation via heterogeneous nucleation was analyzed.

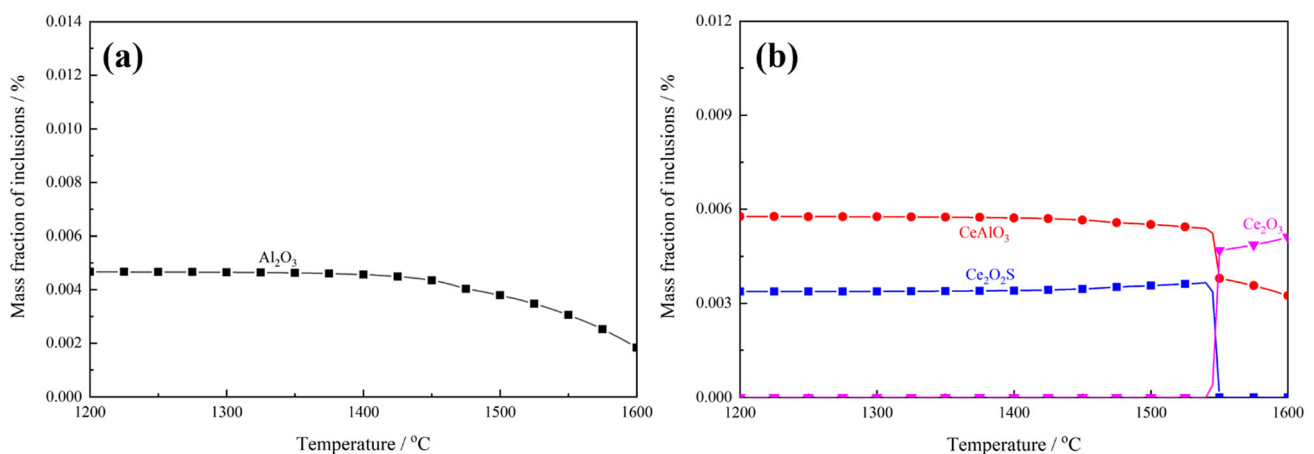


**Fig. 9** Equilibrium precipitation of inclusions in steel between 1200 and 1600 °C calculated using FactSage 8.0 for ingot A (a) and ingot B (b)

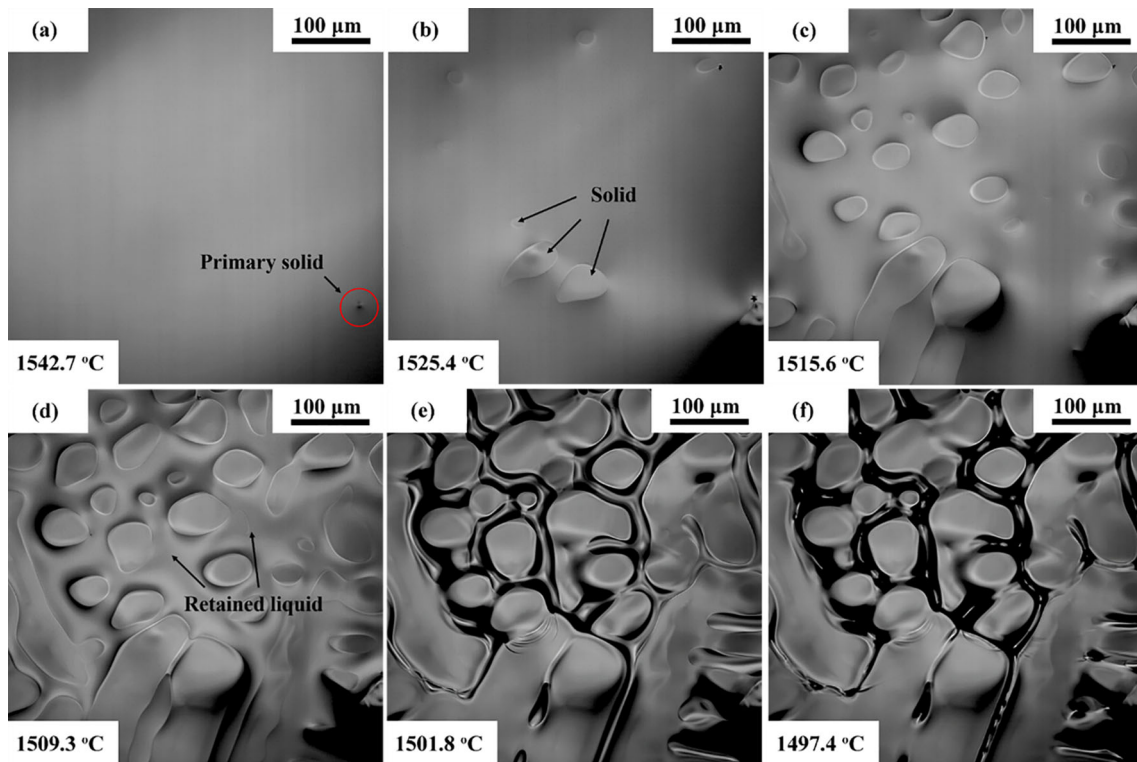


Fig. 10 HTCLSM images of solidification process exhibited by ingot A

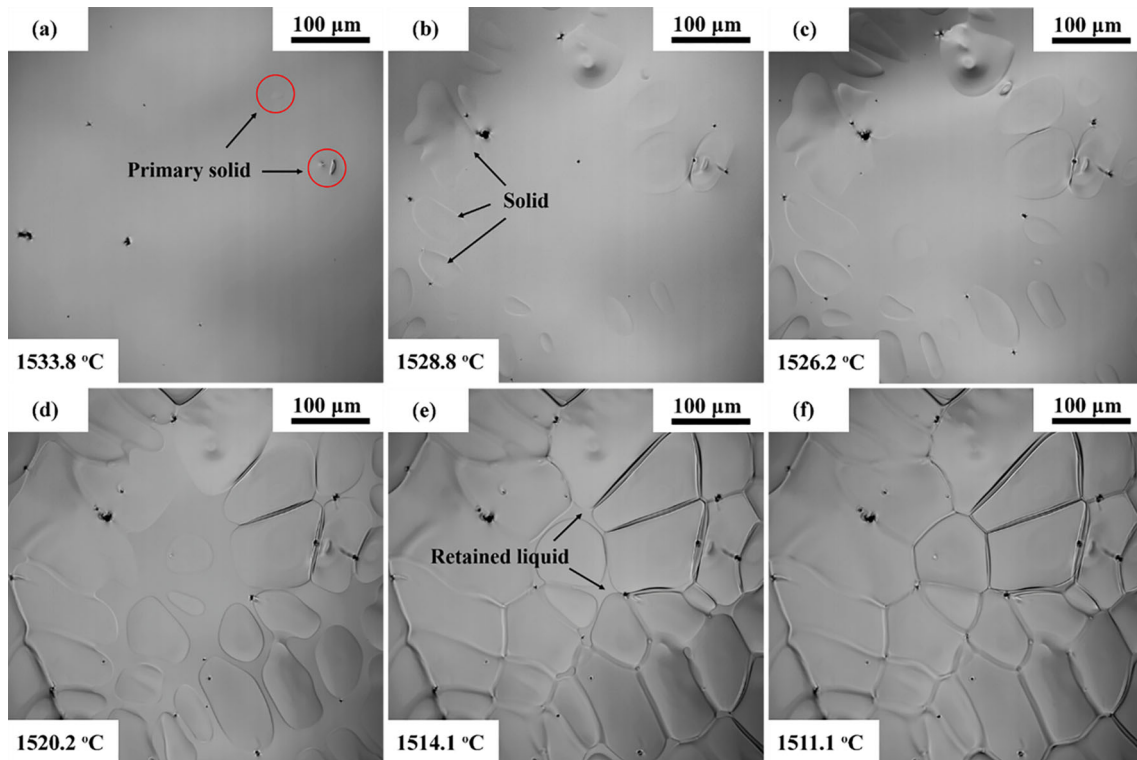


Fig. 11 HTCLSM images of solidification process exhibited by ingot B

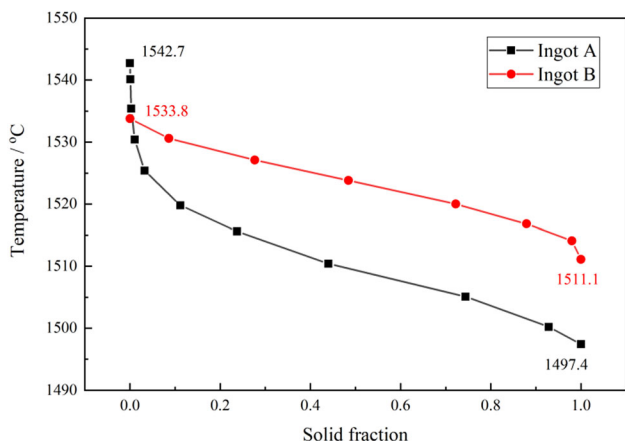


Fig. 12 Solid fraction change exhibited by ingots A and B during solidification

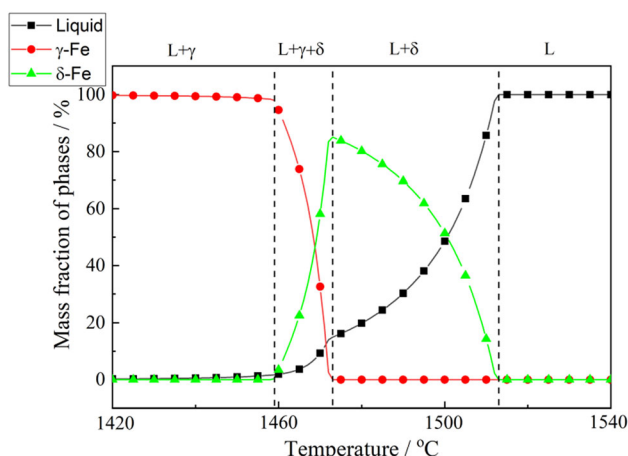


Fig. 13 Solidification path of ingot A between 1420 and 1540 °C

The ability of inclusions to promote  $\delta$ -Fe formation via heterogeneous nucleation primarily depends on three conditions. Firstly, the melting temperature of the inclusion must be higher than the liquidus temperature of the steel. The melting temperatures of  $\text{Al}_2\text{O}_3$ ,  $\text{CeAlO}_3$ , and  $\text{Ce}_2\text{O}_2\text{S}$  are 2020, 2031, and 1950 °C, respectively [24]. Each of these temperatures exceeded the liquidus temperature of the steel used in this study. Secondly, the inclusion must remain in a stable state throughout solidification, as illustrated in the thermodynamic calculation which pertains to the inclusion formation. Finally, there should be a suitable epitaxial fit between the inclusion and  $\delta$ -Fe, as discussed in the Bramfitt disregistry theory and expressed by the following equation [25].

$$\Delta_{(hkl)_s}^{(hkl)_n} = \sum_{i=1}^3 \frac{|d_{[uvw]_s}^i \cos \theta - d_{[uvw]_n}^i|}{3} \times 100 \quad (2)$$

where  $i$  represents three lowest-index directions within a 90° quadrant of the planes of the nucleated solid and

substrate;  $(hkl)_s$  corresponds to the low-index plane of the substrate;  $(hkl)_n$  corresponds to a low-index plane of the nucleated solid;  $[uvw]_s$  corresponds to a low-index direction of  $(hkl)_s$ ;  $[uvw]_n$  corresponds to a low-index direction of  $(hkl)_n$ ;  $d_{[uvw]_n}$  corresponds to the interatomic spacing along  $[uvw]_n$ ;  $d_{[uvw]_s}$  corresponds to the interatomic spacing along  $[uvw]_s$ ; and  $\theta$  corresponds to the angle formed between  $[uvw]_s$  and  $[uvw]_n$ .

To perform the disregistry calculation, the three-dimensional lattice structures exhibited by  $\text{Al}_2\text{O}_3$ ,  $\text{CeAlO}_3$ , and  $\text{Ce}_2\text{O}_2\text{S}$  were established, as shown in Fig. 14. The lattice system and parameters corresponding to the relevant substrate and nucleated solid are listed in Table 2.

The (0001), (0001), and (001) planes of the  $\text{Al}_2\text{O}_3$ ,  $\text{Ce}_2\text{O}_2\text{S}$ , and  $\text{CeAlO}_3$  inclusions were selected as the respective nucleating planes. Three low-index planes of  $\delta$ -Fe, (110), (100), and (111), were used as the mating planes. The minimal disregistry values were obtained based on the orientation relationships exhibited by (0001) $\text{Al}_2\text{O}_3$ //(111) $\delta$ -Fe, (0001) $\text{Ce}_2\text{O}_2\text{S}$ //(111) $\delta$ -Fe and (001) $\text{CeAlO}_3$ //(111) $\delta$ -Fe, as shown in Fig. 15, while the corresponding disregistry results are listed in Table 3.

Bramfitt proposed that a substrate is most effective in promoting the nucleation of a nucleated solid when the disregistry value is less than 6%. According to the parameters listed in Table 3,  $\text{Ce}_2\text{O}_2\text{S}$  is more effective for promoting the formation of  $\delta$ -Fe in comparison to both  $\text{Al}_2\text{O}_3$  and  $\text{CeAlO}_3$  inclusion. In addition to the crystallographic matching between the nucleant particles and the matrix material, the size and number of the nucleant

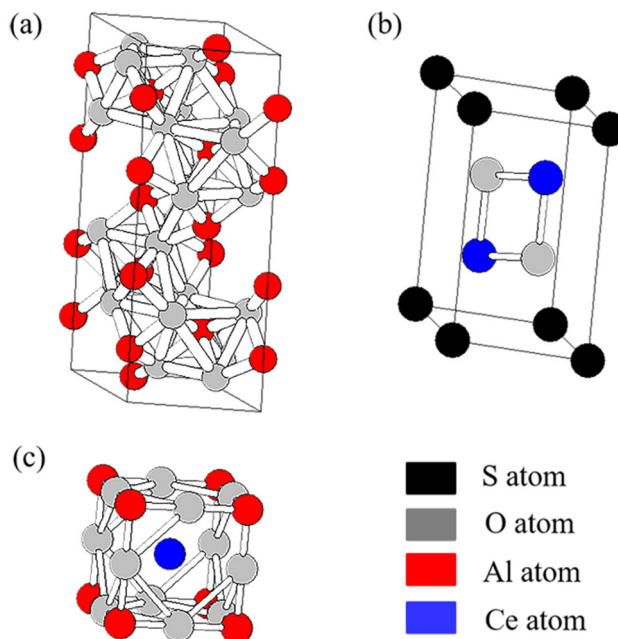
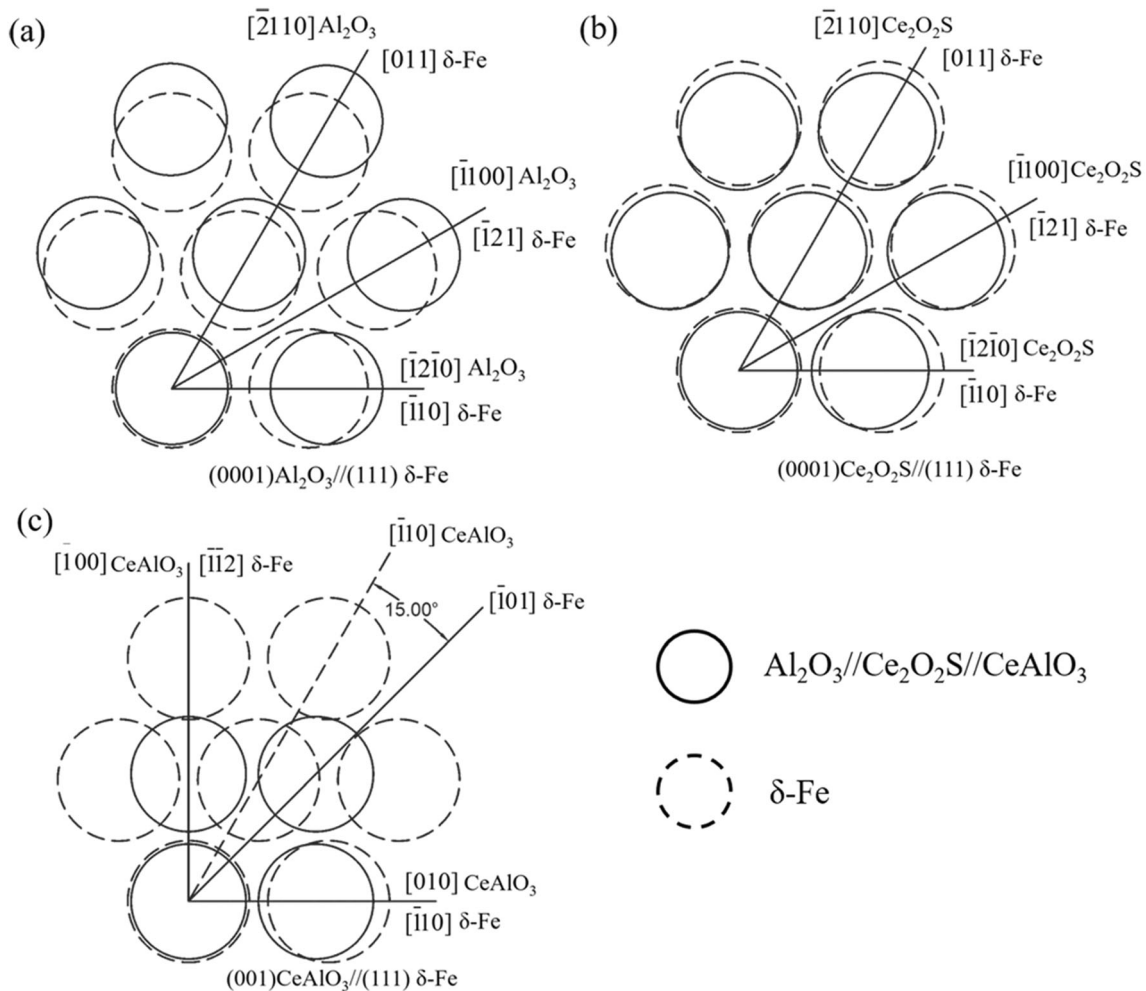


Fig. 14 Three-dimensional lattice structures exhibited by different inclusions. a  $\text{Al}_2\text{O}_3$ ; b  $\text{Ce}_2\text{O}_2\text{S}$ ; c  $\text{CeAlO}_3$



**Table 2** Lattice system and parameters of substrate and nucleated solid

Substance	$\delta$ -Fe	$\text{Al}_2\text{O}_3$	$\text{Ce}_2\text{O}_2\text{S}$	$\text{CeAlO}_3$
Space group	$I\bar{m}\bar{3}m$	$R\bar{3}cH$	$P\bar{3}m1$	$P4/mmm$
Lattice parameter/nm	$a = 0.29315$	$a = 0.4754, c = 1.299$	$a = 0.401, c = 0.693$	$a = b = 0.37669, c = 0.37967$



**Fig. 15** Orientation relationship between  $\text{Al}_2\text{O}_3$  (a),  $\text{Ce}_2\text{O}_2\text{S}$  (b), and  $\text{CeAlO}_3$  (c) and  $\delta$ -Fe

**Table 3** Disregistry calculation results exhibited between inclusions and  $\delta$ -Fe (%)

Inclusions	$\text{Al}_2\text{O}_3$	$\text{Ce}_2\text{O}_2\text{S}$	$\text{CeAlO}_3$
Disregistry results	14.67	3.28	26.93
Disregistry results	14.67	3.28	26.93

particles also play a crucial role in grain refinement [26, 27]. Therefore, the formation of a large number of

finer  $\text{Ce}_2\text{O}_2\text{S}$  inclusions results in the considerable promotion of  $\delta$ -Fe formation via heterogeneous nucleation, thus increasing the equiaxed grain ratio exhibited by the as-cast microstructure while simultaneously reducing the solidification temperature range.

### 4 Conclusions

1. In the case of the steel used in this study, the typical inclusions observed in the ingot without Ce addition

were composed of  $\text{Al}_2\text{O}_3$  inclusions. Upon the addition of Ce, both  $\text{Ce}_2\text{O}_3$  and  $\text{CeAlO}_3$  inclusions were formed, exhibiting a significantly finer size and increased number density.

2. A reduction in the segregation and a corresponding increase in the homogeneous carbon distribution were imparted through the addition of Ce. The results of the in situ observation of solidification indicated that the Ce addition significantly reduced the solidification temperature range, thus limiting carbon segregation.
3. A larger equiaxed zone was obtained through the addition of Ce, while the nucleation effect imparted by  $\text{Al}_2\text{O}_3$ ,  $\text{Ce}_2\text{O}_3$ , and  $\text{CeAlO}_3$  on  $\delta$ -Fe formation was discussed in the context of the disregistry theory. The results show that the disregistry between  $\text{Ce}_2\text{O}_3$  and  $\delta$ -Fe was 3.28%, suggesting a beneficial effect on the promotion of  $\delta$ -Fe formation. Therefore, the formation of a significant number of fine Ce-containing inclusions also promoted  $\delta$ -Fe formation via heterogeneous nucleation, thus increasing the equiaxed grain ratio exhibited by the as-cast microstructure, which, in return, reduced the solidification temperature range and improved the carbon segregation.

**Acknowledgements** The authors are grateful for the financial support of the National Natural Science Foundation of China (No. 52074026).

## References

- [1] G.L. Liang, S.W. Yang, H.B. Wu, X.L. Liu, *Rare Met.* 32 (2013) 129–133.
- [2] M.Z. Jiang, Y.C. Yu, H. Li, X. Ren, S.B. Wang, *High Temp. Mater. Process.* 36 (2016) 145–153.
- [3] C.B. Shi, D.L. Zheng, B.S. Guo, J. Li, F. Jiang, *Metall. Mater. Trans. B* 49 (2018) 3390–3402.
- [4] J.H. Park, H. Todoroki, *ISIJ Int.* 50 (2010) 1333–1346.
- [5] C.B. Shi, W.T. Yu, H. Wang, J. Li, M. Jiang, *Metall. Mater. Trans. B* 48 (2017) 146–161.
- [6] Y. Tabatabaei, K.S. Coley, G.A. Irons, S. Sun, *Metall. Mater. Trans. B* 49 (2018) 375–387.
- [7] Q. Ren, L.F. Zhang, *Metall. Mater. Trans. B* 51 (2020) 589–600.
- [8] G. Thewlis, *Mater. Sci. Tech.* 22 (2006) 153–162.
- [9] Y.X. Cao, X.L. Wan, Y.H. Hou, C.R. Niu, Y. Liu, G.Q. Li, *Steel Res. Int.* 90 (2019) 1900084.
- [10] X.P. Ma, X.D. Li, B. Langelier, B. Gault, S. Subramanian, L. Collins, *Metall. Mater. Trans. A* 49 (2018) 4824–4837.
- [11] Q. Wang, L.J. Wang, Y.H. Sun, A.M. Zhao, W. Zhang, J.M. Li, H.B. Dong, K. Chou, *J. Alloy. Compd.* 815 (2020) 152418.
- [12] H. Torkamani, S. Raygan, C.G. Matro, J. Rassizadehghani, Y. Palizdar, D. San-Martin, *Met. Mater. Int.* 24 (2018) 773–788.
- [13] M.X. Guo, H. Suito, *ISIJ Int.* 39 (1999) 678–686.
- [14] C.V.D. Eijk, Ø. Grong, F. Haakonsen, L. Kolbeinsen, G. Tranell, *ISIJ Int.* 49 (2009) 1046–1050.
- [15] J.Z. Gao, P.X. Fu, H.W. Liu, D.Z. Li, *Metals* 5 (2015) 383–394.
- [16] Y.Y. Hou, G.G. Cheng, *Metall. Mater. Trans. B* 50 (2019) 1322–1333.
- [17] D.W. Zhao, H.B. Li, Y. Cui, J. Yang, *ISIJ Int.* 56 (2016) 1181–1187.
- [18] W. Yang, L.F. Zhang, X.H. Wang, Y. Ren, X.F. Liu, Q.L. Shan, *ISIJ Int.* 53 (2013) 1401–1410.
- [19] N. Verma, P.C. Pistorius, R.J. Fruehan, M. Potter, M. Lind, S.R. Story, *Metall. Mater. Trans. B* 42 (2011) 720–729.
- [20] Y.K. Yang, D.P. Zhan, H. Lei, G.X. Qiu, Y.L. Li, Z.H. Jiang, H.S. Zhang, *Metall. Mater. Trans. B* 50 (2019) 2536–2546.
- [21] I. Ohnaka, *Trans. ISIJ* 26 (1986) 1045–1051.
- [22] Q.P. Dong, J.M. Zhang, L. Qian, Y.B. Yin, *ISIJ Int.* 57 (2017) 814–823.
- [23] Y.Y. Hou, G.G. Cheng, *Metall. Mater. Trans. B* 50 (2019) 1351–1364.
- [24] L.A. Simirnov, V.A. Rovnushkin, A.S. Oryshchenko, G.Y. Kalinin, V.G. Milyuts, *Metallurgist* 59 (2016) 1053–1061.
- [25] B.L. Bramfitt, *Metall. Trans.* 1 (1970) 1987–1995.
- [26] A.L. Greer, A.M. Bunn, A. Tronche, P.V. Evans, D.J. Bristow, *Acta Mater.* 48 (2000) 2823–2835.
- [27] T.E. Quisted, A.L. Greer, *Acta Mater.* 52 (2004) 3859–3868.